crystals

MDPI

Article

Enhanced Dielectric Response and Electric Field-Sensing Properties of PDMS Composites by Graphene/Nitride Heterojunctions: Insights from Experiment and DFT

Bo Li [1,2], Jiao Sun [3], Yuxing Lei [1,2], Tingting Jiang [1] and Haitao Yang [4,*]

[1] Electric Power Research Institute of Yunnan Power Grid Co., Ltd., Kunming 650217, China
[2] Yunnan Provincial Key Laboratory of Green Energy and Digital Power Measurement, Control and Protection, Kunming 650217, China
[3] Kunming Power Supply Bureau of Yunnan Power Grid Co., Ltd., Kunming 650217, China
[4] School of Electrical Engineering, Beijing Jiaotong University, Beijing 100044, China
* Correspondence: 20117010@bjtu.edu.cn

Abstract

Flexible dielectric composite materials capable of converting power frequency electric fields into measurable electrical signals are of great significance in the field of non-contact electric field sensing in power systems. In this paper, graphene/nitride heterojunction powders were prepared using three representative nitrides (AlN, BN, and Si_3N_4) and embedded in polydimethylsiloxane (PDMS) to prepare flexible composite films with a fixed filler content of 5.0 wt%. Scanning electron microscopy (SEM) and energy dispersive spectroscopy (EDS) confirmed the successful formation of the heterojunctions. The results showed that the nitride-related elements (Al, Si and N) were spatially correlated with the graphene-rich regions, thus providing abundant interfacial contact sites. Dielectric spectroscopy (50 Hz–50 kHz) showed that all samples exhibited typical dispersive behavior, with the real part of the dielectric constant decreasing monotonically with increasing frequency, and the loss tangent also decreasing smoothly. Under a 50 Hz parallel-plate electric field, the normalized induced voltage amplitude (PDMS = 1) increases to 1.070 (≈7.0%) for G/PDMS, and further to 1.0723–1.07447 (≈7.23–7.45%) for AlN–G/PDMS, BN–G/PDMS, and Si_3N_4-G/PDMS. DFT calculations confirm that the graphene/nitride interface has a stable structure with negative binding energies (−2.241, −1.773, and −3.062 eV for AlN–G, BN–G, and Si_3N_4–G, respectively). Significant charge redistribution and Mulliken charge transfer (0.0538, 0.2047, and 0.0244 eV, respectively) are present at the interface, accompanied by Fermi level density of states modulation and a small bandgap opening (~0.101 eV) in BN–G. These results collectively support the interfacial polarization-driven mechanism and provide a comparative basis for selecting nitride components in graphene-based heterojunction fillers in flexible dielectric electric field-sensing layers.

Keywords: graphene; nitrides; heterojunction; PDMS composites; electric field sensing; DFT

Check for updates

Academic Editor: Dah-Shyang Tsai

Received: 10 December 2025
Revised: 28 January 2026
Accepted: 7 February 2026
Published: 11 February 2026

Copyright: © 2026 by the authors. Licensee MDPI, Basel, Switzerland. This article is an open access article distributed under the terms and conditions of the Creative Commons Attribution (CC BY) license.

1. Introduction

Accurate electric field monitoring plays a crucial role in the safe operation of power systems, especially in locations where direct contact with electricity is inconvenient, such as high-voltage transmission lines and substations. Against this backdrop, non-contact electric field measurement strategies based on electric field coupling have attracted considerable attention due to their ability to estimate potentials without electrical connections, and their

potential to improve personnel safety and ease of installation [1]. The increasing demand for lightweight sensing layers (such as those for bent conductors, insulating housings, or compact measuring heads) is driving the development of sensing materials towards flexible polymer dielectrics, where the electric field induced signal is closely related to polarization capability and interfacial charge dynamics [2,3].

Polydimethylsiloxane (PDMS) is widely used as a flexible dielectric platform due to its good processability, mechanical flexibility, and chemical stability. However, the relatively low dielectric constant of PDMS alone limits the induced charge density, thus limiting the output signal obtainable under a given external field. A common method to enhance the dielectric response of polymers is to introduce functional fillers to form polymer composites with enhanced polarization processes. In such composites, dielectric behavior is typically influenced not only by the intrinsic dielectric constants of each phase but also by interfacial polarization, particularly the Maxwell-Wagner-Silas (MWS) effect caused by charge accumulation at the heterojunction [4–6]. For conductive filler composites, percolation microstructures can significantly improve the effective dielectric constant but may also increase dielectric loss and lead to leakage paths, thus creating a trade-off between signal enhancement and stability [7]. Two-dimensional (2D) materials offer attractive tools for interfacial polarization modulation due to their large specific surface area and tunable electronic structure. Graphene, in particular, has been extensively studied as a conductive nanofiller in polymers, where its high carrier mobility and sheet-like structure can enhance MWS polarization at low filler contents while maintaining mechanical flexibility [8,9]. Recent advances in "hybrid 2D systems" beyond simple dispersion suggest that heterojunction structures can be used as design parameters to modulate charge transfer and polarization centers, rather than solely depending on filler concentration [10]. This interface engineering concept suggests that cleverly combining graphene with a second wide-bandgap material component can achieve more controllable interfacial charge trapping or relaxation, thereby improving dielectric response with a moderate increase in loss.

Among wide-bandgap candidate materials, nitride ceramics are particularly important in power and electronic applications due to their excellent thermal/chemical stability, high breakdown strength, and strong insulation properties. Therefore, nitride-filled polymer composites (such as BN, AlN, and Si_3N_4-based systems) have been extensively studied and reported to enhance dielectric stability, typically through improved dielectric breakdown strength and modulation of interfacial charge/space charge behavior [11–14]. In particular, boron nitride nanosheets provide an electrically insulating two-dimensional filler platform with a large interfacial area, enabling effective modulation of the interface in polymer composites. Notably, BN, AlN, and Si_3N_4 differ in electronegativity, polarization tendency, and electron affinity, meaning that even with the same polymer matrix and similar filler content, graphene/nitride heterointerfaces may exhibit different charge redistribution and relaxation characteristics [15]. Importantly, these nitrides also differ in electronegativity, polarization tendency, and electron affinity, meaning that even with the same polymer matrix and similar filler content, the graphene/nitride interface may exhibit different charge redistribution behaviors. From an electronic structure perspective, graphene on hexagonal boron nitride (HBN) is a typical heterostructure where inversion symmetry breaking and interfacial coupling can open a small band gap and alter the carrier distribution near the Fermi level [16–18]. Related theoretical studies further indicate that graphene interfaced with 2D nitride layers (BN and AlN-related systems) can exhibit tunable band alignment and interfacial charge transfer, which is expected to influence polarization relaxation under low-frequency alternating electric fields [19–21]. Furthermore, graphene–dielectric nitride combinations have been explored in the device field, such as nitride/graphene dielectric stacks and nitride-related interfaces, highlighting their compatibility in electronic and insu-

lating applications [22–24]. Despite these advances, systematic material-level comparisons of how different nitride species (BN, AlN, Si_3N_4) modulate graphene-based heterointerfaces, and how this modulation translates into the dielectric spectral characteristics and power-frequency electric field-induced outputs of flexible polymer composites remain limited. In practice, composite materials prepared with similar filler contents may exhibit similar dielectric constants and loss curves, but subtle differences in interfacial charge redistribution and relaxation remain important for elucidating mechanisms and guiding subsequent optimizations (filler ratios, dispersion strategies, stacking sequences, or surface treatments). Therefore, a combined experimental and theoretical approach is needed to address the following questions: microstructural evidence for heterogeneous interface formation, frequency-dependent dielectric response controlled by interfacial polarization, and voltage output induced by a direct electric field under a controlled uniform electric field [25].

This study prepared graphene/nitride heterojunction powders using three representative nitrides (AlN, BN, and Si_3N_4) and embedded them in polydimethylsiloxane (PDMS) to form flexible dielectric composite films with fixed filler content for fair comparison. The heterojunction powders were characterized using scanning electron microscopy (SEM) and energy-dispersive X-ray spectroscopy (EDS) to confirm their morphology and elemental distribution. Subsequently, the dielectric constant and dielectric loss tangent were measured in the low-frequency range associated with polarization relaxation, and the electric field-induced voltage output was evaluated under an alternating power frequency electric field using a parallel plate field generation system. To elucidate the sources of differences among the different nitrides, density functional theory (DFT) calculations were performed to obtain optimized interface configurations, binding energies, charge density differences, and electronic structures (band structures and density of states). This study aims to provide a structure-performance framework for designing graphene/nitride-polymer composites for flexible electric field-sensing layers by correlating interfacial charge redistribution with dielectric spectral trends and induced output.

2. Experimental and DFT Calculation Methods

2.1. Material Synthesis

Graphene nanosheets and three nitride nanoparticles (AlN, BN, and Si_3N_4), along with all other reagents, were purchased from Aladdin Reagents Co., Ltd. (Shanghai, China). The heterojunctions formed by the three nitrides and graphene were obtained using a hydrothermal method. The preparation process of the heterojunctions composed of the three nitrides and graphene was the same, except for the pH conditions used in the experiments. For example, the formation of heterojunctions between AlN and Si_3N_4 nanoparticles and graphene required pH = 5, while the formation of heterojunctions between BN nanoparticles and graphene required neutral conditions (pH = 7). The preparation process of the AlN-G heterojunction material is described in detail below as an example: 0.5 g of AlN was dispersed in 30 mL of deionized water and magnetically stirred for 30 min at room temperature to form a homogeneous suspension. Then, 0.5 g of graphene was slowly added to the suspension, and stirring was continued for 1 h to ensure uniform mixing of the two substances. Then, 0.1 mol/L dilute hydrochloric acid was added to adjust the pH of the mixture to 5.0 ± 0.1. The mixture was transferred to a 100 mL polytetrafluoroethylene-lined reactor (KH-100, Gongyi Yuhua Instrument Co., Ltd., Gongyi, China). After sealing the reactor, it was placed in a constant temperature (DHG-9070A, Shanghai Yiheng Scientific Instrument Co., Ltd., Shanghai, China) oven at 180 °C for 12 h. After the heating reaction was completed, the reactor was removed and allowed to cool naturally to room temperature. The lower precipitate was immediately collected. The collected precipitate was washed

and centrifuged at 8000 rpm, and washed three times with deionized water and anhydrous ethanol, respectively. Finally, the powder was treated in a vacuum drying (DZF-6050, Shanghai Yiheng Scientific Instrument Co., Ltd., Shanghai, China) oven at 60 °C for 12 h to obtain AIN-G heterojunction powder. The entire synthesis process is shown in Figure 1.

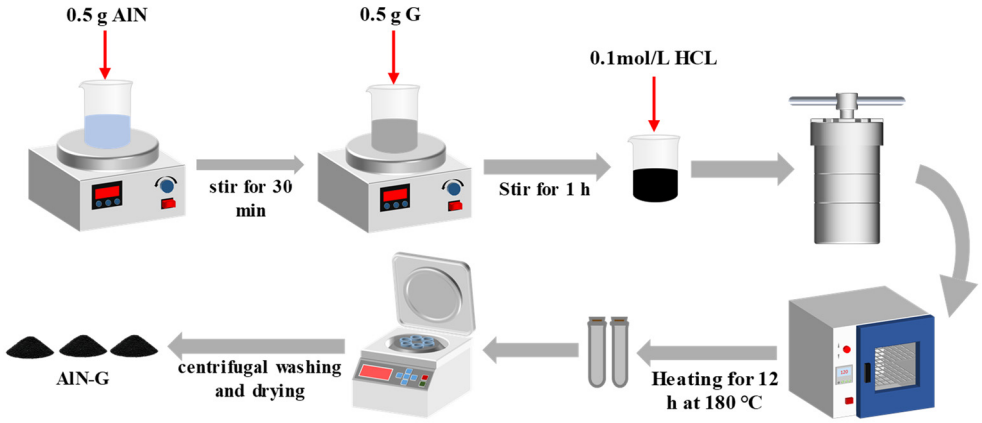

Figure 1. Preparation process of graphene and AIN heterojunction Materials.

Composite films composed of graphene-nitride heterojunction powder and PDMS were prepared by solution blending. PDMS matrix and curing agent (Sylgard 184) were mixed at a mass ratio of 10:1, and then the synthesized graphene-nitride heterojunction powders (AlN-G, BN-G, and Si_3N_4-G) were added to the PDMS mixture. To ensure a fair comparison of the inherent properties of different heterojunction fillers, the heterojunction powder filler content in all composite samples was fixed at 5 wt%. The mixture was mechanically stirred for 30 min, followed by ultrasonic treatment for 1 h to achieve uniform dispersion of the filler. Finally, the mixture was degassed in a vacuum to remove residual bubbles and cured in an oven at 80 °C for 2 h to obtain a flexible composite film, as shown in Figure 2.

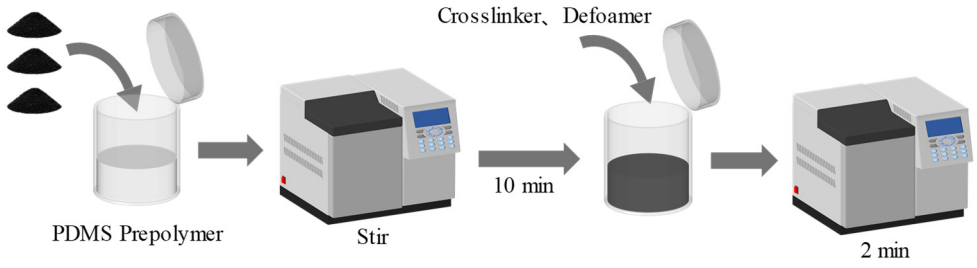

Figure 2. Preparation Process of PDMS Composite Film.

2.2. Materials Characterisation

To thoroughly investigate the morphological features and elemental distribution of the functional fillers, the microstructure was systematically characterized using a Zeiss Gemini SEM 300 field emission scanning electron microscope (SEM, Carl Zeiss AG, Oberkochen, Germany) equipped with an Oxford Instruments Xplore 30 energy-dispersive X-ray spectroscopy (EDS, Oxford Instruments plc, Abingdon, UK) system. The sample preparation followed a specific protocol to ensure high-quality imaging. The synthesized heterojunction powders were dispersed in anhydrous ethanol and subjected to ultrasonic treatment for 15 min to achieve a homogeneous suspension. An aliquot of the dispersion was then drop-cast onto the sample stage and dried at ambient temperature. To enhance surface conductivity and prevent charging effects during imaging, a Au/Pd alloy coating (approx-

imately 5 nm thick) was deposited onto the sample surface using a Leica-EM ACE600 high-vacuum ion sputtering instrument (Leica Microsystems GmbH, Wetzlar, Germany).

2.3. Dielectric Spectroscopy and Electric Field-Sensing Tests

Dielectric spectrum measurements were performed using a centralized circuit method. To minimize capacitance artifacts caused by interfacial air gaps, flexible copper foil contact electrodes were used during the test. The electrodes were made of double-sided conductive copper strips with a diameter of 30 mm. A Tonghui TH2830 LCR digital bridge (Tonghui Electronic Co., Ltd., Changzhou, China) equipped with a dedicated fixture was used as the main instrument for capacitance and loss measurements. Auxiliary equipment included a high-precision miniature thickness gauge (model TDGC2-5 kVA, Tianjin Tianshi Power Supply Co., Ltd., Tianjin, China) for accurate thickness measurement and a vacuum drying (DZF-6050, Shanghai Yiheng Scientific Instrument Co., Ltd., Shanghai, China) oven for sample pretreatment before measurement. The sample preparation process for dielectric measurement was as follows: First, a PDMS184 release agent was sprayed onto a glass substrate, and then a uniform film with a thickness of 100 ± 10 μm was coated using a wire rod coater. After vacuum curing at 80 °C for 2 h, the cured film was immersed in an 80 °C water bath and gently peeled off from the glass substrate with the aid of the release agent. The film was then cut into 40 mm × 40 mm square samples. To construct a standard parallel-plate capacitor structure, 30 mm diameter circular double-sided conductive copper tapes were attached as electrodes at the geometric center on both sides of each sample to ensure tight contact between the electrodes and the film surface without any air bubbles. To evaluate the effect of heterojunction fillers, five material samples were prepared using the same procedure: pure PDMS, G/PDMS, AIN–G/PDMS, BN–G/PDMS, and Si_3N_4–G/PDMS. G/PDMS was used as a control to evaluate the effect of heterojunction engineering. Dielectric measurements were performed in logarithmic mode, with a frequency scan range of 50 Hz to 50 kHz, recording five data points every ten octaves. An AC excitation voltage of 1.0 Vrms was applied. Before testing, the sample thickness was measured at three locations using a miniature thickness gauge, and the average value was used for subsequent calculations. The samples were then clamped in a tweezers clamp for automated frequency scanning measurements, and the dielectric data were recorded. During the measurement, the capacitance (C), dissipation factor (D), and phase angle were directly recorded by the LCR digital bridge at each frequency point. The relative dielectric constant (ε) of the composite films was calculated using Equation (1), where d is the sample thickness, ε_0 represents the vacuum dielectric constant (8.85×10^{-12} F/m), and A^{etest} is the electrode area.

$$\varepsilon = \frac{Cd}{\varepsilon_0 A} \tag{1}$$

The electric field-induced response of the prepared composite thin film was characterized using a parallel-plate AC electric field platform (custom-built, Kunming, China). This device provides a stable and spatially uniform electric field and can quantitatively record the induced voltage output of the film, thus supporting its potential application in electric field measurements. The platform includes an electric field generator, a sample/sensor holder, and a signal readout unit. The electric field generator uses two circular aluminum plates (500 mm in diameter) as parallel electrodes. The upper electrode is driven by an adjustable 50 Hz high-voltage AC excitation generated by a programmable AC power supply and a step-up transformer, while the lower electrode is grounded through a protective resistor. A custom-designed three-electrode holder (including a calibration electrode) is used to mount the film, allowing for rapid installation/removal and simultaneous measurement of multiple samples when needed. All measurements were performed under stress-free conditions (i.e., no external mechanical pressure on the film). Signal acquisi-

tion was performed using a multi-channel digital oscilloscope (TBS1102, Tektronix Inc., Beaverton, OR, USA). The applied electrode voltage was monitored using a high-voltage differential probe (DP-50, Pintek Electronics Co., Ltd., New Taipei City, Taiwan), while the induced response signal from the sensor holder was acquired using a high-impedance single-ended probe (P6139B, Tektronix Inc., Beaverton, OR, USA) and transmitted to a computer for post-processing. During the measurement, the electric field strength was adjusted by regulating the high-voltage excitation, allowing the electric field strength to scan from 0 to 5 kV/cm at a fixed frequency of 50 Hz. The electric field strength was determined according to Equation (2), where V is the instantaneous voltage difference between the two electrodes (measured by the high-voltage differential probe), and the $d1$ is the fixed electrode spacing. Before the formal test, a blank experiment (without any sample placed) was first performed to record the baseline signal and eliminate the effects of parasitic capacitance and environmental electromagnetic interference. The test sample was then placed in the central region (uniform field region) of the electrode array and fixed with a mechanical clamp before the test began. The experimental setup and measurement procedure are shown in Figure 3.

$$E = \frac{V}{d1} \tag{2}$$

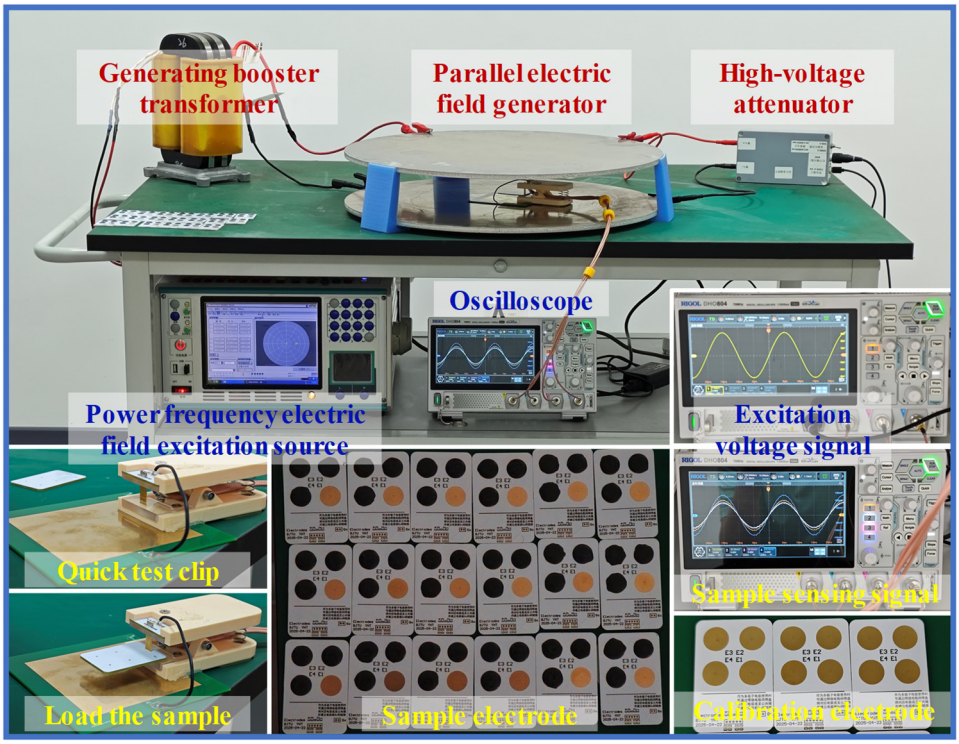

Figure 3. Experimental process diagram of electric field-sensing performance test.

2.4. DFT Calculations Method

Based on the First Principles theory, geometric optimization and energy calculation were carried out using the Dmol3 program in the Material Studio 2019 (MS) software package [26,27]. The electron exchange correlation interaction is handled using the Perdew-Burke-Ernzerhof (PBE) functional under the generalized gradient approximation [28,29]. In the calculation of nuclear electronics and electronic pseudopotentials, DFT semi-nuclear pseudopotentials and dual numerical basis sets plus polarization functions were adopted [30]. The dispersion corrections such as van der Waals forces and long-range interactions were considered through the DFT method [31,32]. In the Brillouin zone, the

K-point sampling for geometric optimization and electronic structure calculation is set to $7 \times 7 \times 1$. The energy convergence accuracy, maximum force and maximum displacement are respectively set as 10^{-5} Ha, 2×10^{-3} Ha/A and 5×10^{-3} A [33]. In the static electronic structure field, the global orbital cutoff radius, self-consistent field energy convergence criterion and energy level broadening are set to 5 A, 10^{-6} Ha and 0.005 Ha, respectively [34]. To construct the graphene–nitrides heterojunction models, a $4 \times 4 \times 1$ graphene supercell was generated first, yielding in-plane lattice parameters of a = b = 9.84 Å. For each graphene/nitride interface, commensurate supercells were selected so that the in-plane lattice mismatch remained below 5%. The mismatch was evaluated using Equation (3), where a_1 and a_2 represent the lattice constants of the two lattices to be matched. Accordingly, $3 \times 3 \times 1$ AlN, $4 \times 4 \times 1$ BN, and $2 \times 2 \times 1$ Si_3N_4 supercells were constructed, with lattice constants of 9.385 Å, 10.050 Å, and 12.412 Å, respectively. The calculated mismatch values confirm that all graphene–nitride supercell pairs satisfy the <5% criterion, enabling periodic heterojunction models to be built for subsequent calculations [35]. To balance computational cost and interfacial physics, both graphene and the nitride components were modeled as monolayers. A vacuum spacing of 20 Å was introduced along the c-direction to eliminate interactions between periodic images.

$$\Delta = \frac{2|a_1 - a_2|}{a_1 + a_2} \tag{3}$$

To quantitatively evaluate the interfacial interaction between graphene and the three nitride layers, the binding energy (E_b) was calculated as Equation (4), where E_H is the total energy of the graphene/nitride heterojunction, E_O is the total energy of the isolated nitride layer, and E_G is the total energy of isolated graphene [36].

$$E_b = E_H - E_O - E_G \tag{4}$$

During the formation of heterojunctions between graphene and the three materials mentioned above, charge transfer occurs. The Interfacial charge transfer (Q_t) was evaluated based on Mulliken population analysis, and the magnitude of charge transfer is defined by Equation (5), where Q_a is the Mulliken charge of a given component (graphene or the nitride layer) in the heterojunction, and Q_b is the corresponding Mulliken charge of the same component in the isolated state. The sign of Q_t reflects the charge-transfer direction: a negative Q_t indicates net electron transfer from graphene to the nitride component, whereas a positive Q_t corresponds to electron transfer from the nitride to graphene [37].

$$Q_t = Q_a - Q_b \tag{5}$$

3. Results and Analysis

3.1. Characterization of Material Properties

Figure 4 shows the morphology of three graphene/nitride heterojunction materials at low and high magnification. Despite using the same preparation method, these three fillers exhibit significantly different texture characteristics, indicating that they have different interfacial contact modes during subsequent PDMS embedding. The AlN–G heterojunction material exhibits a typical sheet-like framework and granular decorative morphology. At low magnification, larger graphene sheets form a continuous skeleton, while a large number of bright AlN regions are distributed on the sheet surface, giving the sheets a distinctly rough texture. Under magnification, these AlN regions can be observed to appear as irregular submicron fragments and small sheet-like structures attached to the basal and edge regions. Unlike the formation of isolated blocky AlN clusters, a considerable portion

of AlN is fixed on the graphene, indicating the formation of an effective heterojunction filler with abundant local contact sites. The morphology of the BN–G heterojunction material mainly consists of extended layered sheets with relatively smooth surfaces and distinct stepped edges. Figure 4(B1) shows the stacked sheet-like structures and overlapping flakes, characteristic of layered boron nitride. At high magnification (Figure 4(B2)), the layered stacking structure is more apparent, with smaller flakes covering larger ones, forming broad planar contact areas rather than granular decoration. Compared to the other two heterojunction materials, BN–G exhibits fewer blocky fragments and a more continuous layered texture, consistent with the inherent two-dimensional properties of boron nitride. For the Si_3N_4–G heterojunction material, the images reveal a denser, granular microstructure. Low-magnification images (Figure 4(C1)) show dense aggregates with rough surfaces, composed of densely packed micron/submicron fragments. This aggregated structure is more clearly visible in Figure 4(C2), with irregular sheet-like and blocky particles distributed throughout the field of view. Although some aggregation of the granular nitride components is inevitable, many fragments remain tightly attached near the graphene sheets, resulting in numerous point-to-surface contacts and high-density interface regions.

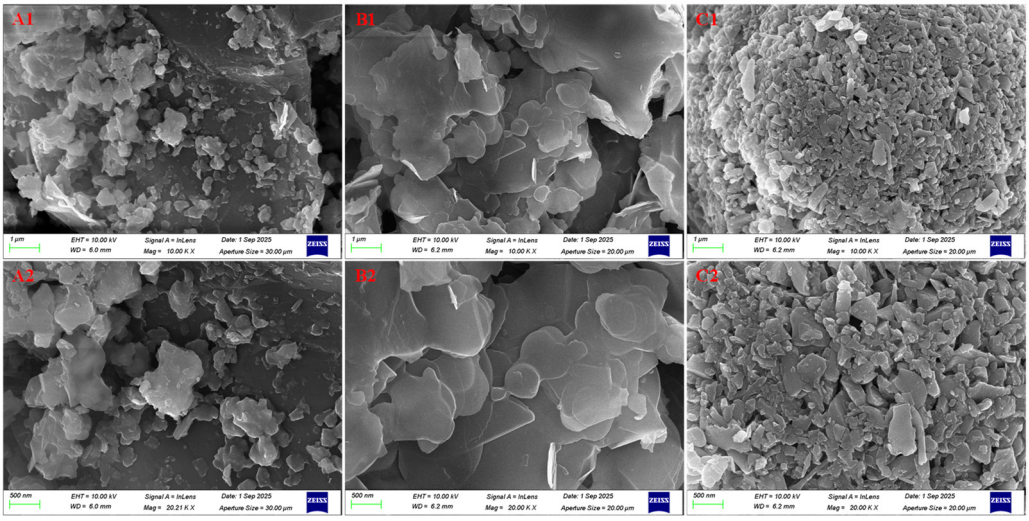

Figure 4. SEM images of graphene/nitrides heterojunction powders at two magnifications. (**A1**,**A2**) AIN-G, (**B1**,**B2**) BN-G, (**C1**,**C2**) Si_3N_4-G. The top row (**A1**–**C1**) shows low-magnification images (scale bar: 1 μm), and the bottom row (**A2**–**C2**) shows high-magnification images (scale bar: 500 nm).

Figure 5 provides EDS spectra and elemental mapping results for the three graphene/nitride heterojunction powders. The EDS spectra (A–C) verify the coexistence of graphene-derived carbon together with the characteristic elements of the corresponding nitride component, confirming the successful incorporation of nitride phases into the graphene-based heterojunction fillers. For AlN–G, the spectrum in Figure 5A is dominated by a strong C peak, accompanied by clear Al signals and a detectable N contribution, which is consistent with the intended AlN-G hybrid composition. The corresponding elemental maps in Figure 5D further illustrate the spatial distribution: the C map delineates the main flake-like framework (graphene-rich region), whereas the Al signal appears broadly distributed across the same field of view, indicating that Al-containing domains are present over and around the graphene framework rather than being completely separated. The N map shows a comparatively weaker intensity, which is expected for light elements in EDS mapping; nevertheless, the N signal is still observable in regions where Al is present, supporting the assignment of AlN-related domains in close proximity to graphene.

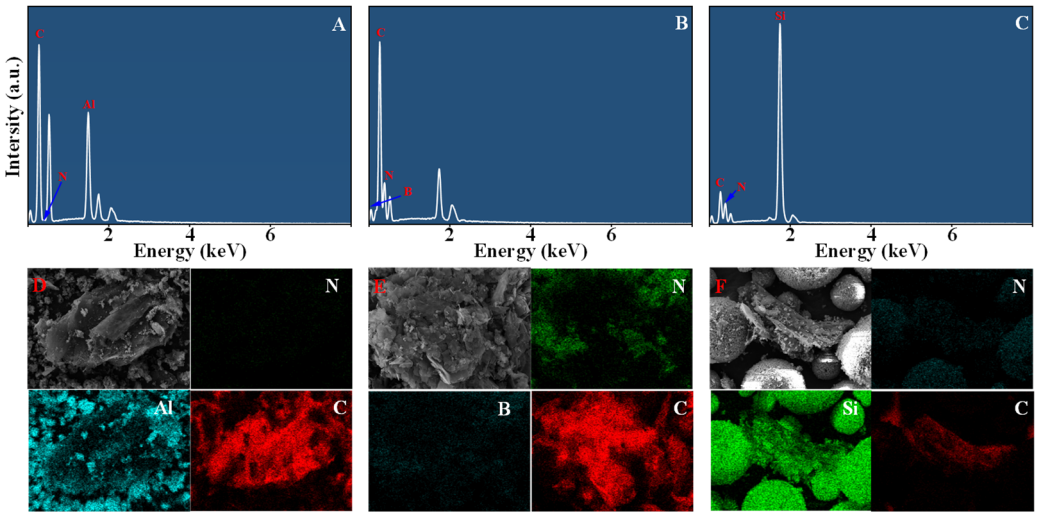

Figure 5. EDS characterization results of graphene/nitrides heterojunction powders. (**A**–**C**) are the EDS spectra of AlN-G, BN-G, and Si_3N_4-G, respectively. (**D**–**F**) are the corresponding SEM im-ages and elemental distribution maps, showing the spatial distribution of N/Al/C, N/B/C, and N/Si/C in AlN-G (**D**), BN-G (**E**), and Si_3N_4-G (**F**), respectively.

A similar consistency is observed for BN–G. In Figure 5B, distinct peaks corresponding to B, N, and C are identified, matching the elemental signature of BN integrated with graphene. In the mapping results (Figure 5E), the C distribution again highlights the graphene-rich scaffold, while B and N signals appear in the same morphological regions, indicating that BN-related domains are not randomly isolated but spatially associated with the graphene structure. Compared with AlN–G, BN–G tends to show a more continuous, sheet-like texture in the SEM image, and the B/N maps exhibit a relatively coherent distribution pattern, consistent with BN's intrinsically layered nature and the formation of extended planar contact regions in the heterojunction filler. For Si_3N_4–G, the EDS spectrum (Figure 5C) shows a pronounced Si peak together with C and N signals, confirming the presence of Si-containing nitride phases within the graphene-based composite powder. The mapping results (Figure 5F) provide a clearer structural picture: the Si (and corresponding N) signals are mainly concentrated on the Si_3N_4-rich domains (appearing as larger particulate features), while the C map is strongly associated with the flake-like component, indicating graphene-rich regions. Notably, the spatial adjacency between the carbon-rich regions and the Si/N-rich domains suggests that the Si particles are assembled together with graphene rather than being completely segregated, thereby creating a high density of local interfacial contact areas.

3.2. Dielectric and Electric-Field Performance Test Results

Figure 6 summarizes the frequency-dependent dielectric behavior and electric field-induced response of pure PDMS and PDMS composites filled with graphene and graphene/nitride heterojunction powders. The overall trend is that both the dielectric constant and loss tangent exhibit significant frequency dispersion, which is common in polymer-based dielectric composites. Within the measured frequency range, the dielectric constant (ε) of all samples gradually decreases with increasing frequency. This monotonic decay reflects typical dielectric dispersion. At low frequencies, dipole orientation in the polymer matrix and interfacial polarization at the filler-matrix interface respond more fully to alternating electric fields, resulting in relatively high ε. As frequency increases, these polarization processes gradually fail to keep up with rapid electric field reversals (relaxation hysteresis), and ε decreases accordingly. Compared to pure PDMS, the introduction of graphene (G/PDMS) causes an overall upward shift in ε values across the entire

frequency range. This enhancement indicates that the conductive two-dimensional filler introduces additional polarization pathways, including micro-capacitor-like interfacial regions and charge accumulation at the graphene-PDMS boundary. After incorporating graphene/nitride heterojunction fillers (AIN-G, BN-G, and Si_3N_4-G), the ε values remained slightly higher than those of pure graphene composites across most frequency ranges. The ε curves of these three heterojunction composites are very close, which is reasonable given their identical PDMS matrix and similar filler content; therefore, the ε profiles appear quantitatively close under the fixed PDMS matrix and uniform 5 wt% loading conditions; however, distinct trend-level nitride-dependent differences are observable. These variations stem from the intrinsic differences in interfacial contact structure and local polarization behavior specific to each nitride.

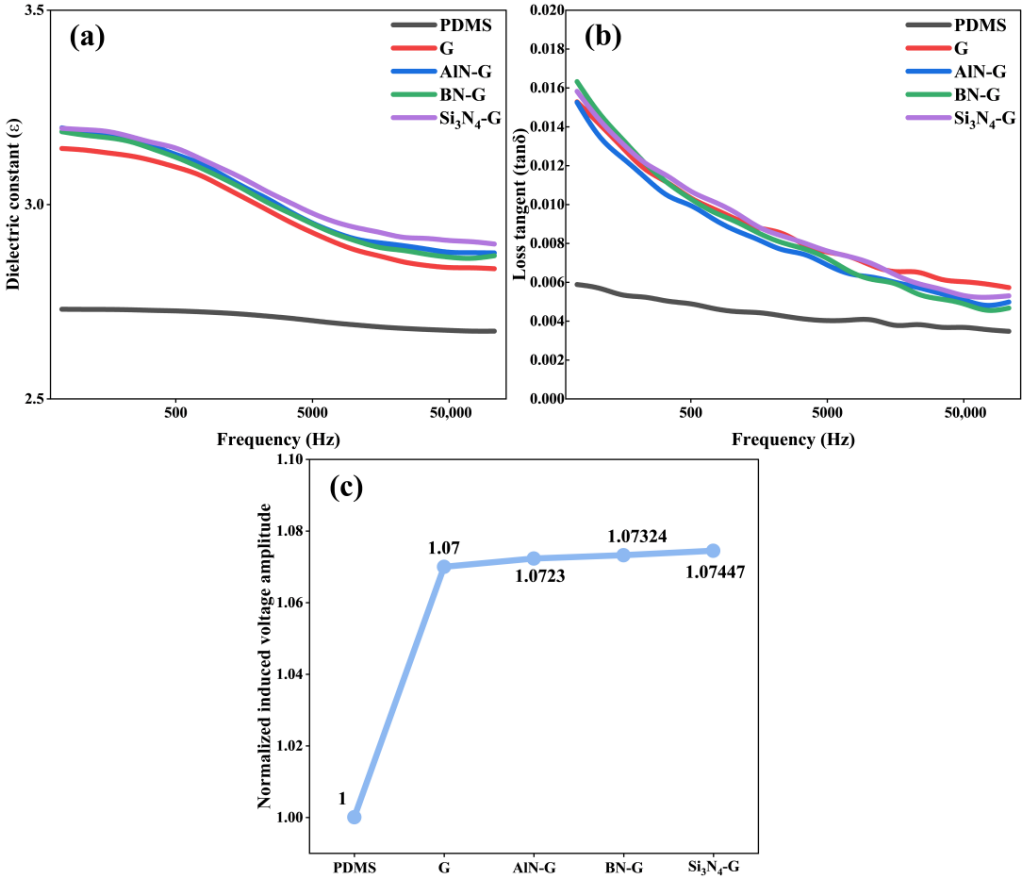

Figure 6. Frequency-dependent dielectric and electric-field response characteristics of pure PDMS and graphene-/heterojunction-filled PDMS composites. (**a**) Real part of the dielectric constant as a function of frequency. (**b**) Dielectric loss tangent as a function of frequency. (**c**) Normalized electric-field-induced voltage amplitude of different samples, with pure PDMS used as the reference (PDMS = 1). Samples include PDMS, graphene/PDMS (G), and graphene/nitrides heterojunction composites (AlN-G, BN-G, and Si_3N_4-G).

Figure 6b shows that the loss tangent (tanδ) of all samples decreases with increasing frequency. The relatively high tanδ values at low frequencies are consistent with a stronger contribution from interfacial relaxation and conduction-related losses, as carriers have sufficient time to migrate and accumulate at the interface. As frequency increases, the efficiency of these processes decreases; thus, the losses gradually decrease. Compared to pure PDMS, the composite material containing graphene and heterojunction filler exhibits a higher tan d value, which is the expected result of introducing more interfacial relaxation paths and charge carriers. Importantly, the loss curves remain smooth without anomalous

peaks, indicating that the introduction of filler did not cause unstable dielectric relaxation behavior or severe leakage paths. Similar to the trend of dielectric constant variation, the tan d curves of AIN-G, BN-G, and Si_3N_4-G are close to each other, indicating that their overall loss behavior is mainly influenced by the common polymer matrix and filler content. Nevertheless, consistent nitride-dependent relaxation characteristics are maintained, confirming that the specific heterojunction interface subtly but distinctively modulates the dielectric loss mechanism.

To directly evaluate the electric field sensing capability, Figure 6c compares the normalized electric field induced voltage amplitudes of different samples, using pure PDMS as a reference (PDMS = 1). Normalization minimizes the differences between devices and highlights the relative contributions of functional fillers under the same testing conditions. Compared to pure PDMS, the graphene-filled composite exhibits a significant performance improvement (normalized voltage amplitude of 1.07), indicating that the introduction of a two-dimensional conductive network and its associated interfacial polarization can enhance the macroscopic sensing response. When using graphene/nitride heterojunction fillers, the normalized induced voltage amplitude is further increased to a slightly higher level (voltage amplitude in the range of 1.07–1.075). Notably, the response levels of the three nitride-based heterojunction composites are very similar, suggesting that the heterojunction structure can provide a consistent enhancement effect. In this high-performance hierarchy, the differences between AlN, BN, and Si_3N_4 exhibit a systematic trend, reflecting the differences in interfacial coupling efficiency driven by specific nitride properties. Among them, the Si_3N_4-G/PDMS composite exhibits the highest response (voltage amplitude of 1.07447), which is 7.447% higher than that of pure PDMS. In summary, the addition of graphene and graphene/nitride heterojunction fillers can increase the interfacial polarization density and promote charge accumulation at the heterojunction interface, which is reflected in the increase in dielectric constant and the improvement in the electric field-induced voltage response. Simultaneously, the overall dielectric loss remains within a controllable range and decreases with frequency, consistent with the typical dielectric behavior of polymer composites.

3.3. Analysis of Computational Results

Figure 7 illustrates the optimized configuration and interfacial charge redistribution characteristics of the graphene/nitride heterostructures obtained through DFT calculations. The top view shows that the optimized nitride layer can be stably assembled on graphene without significant structural collapse or severe distortion of the graphene lattice. This indicates that interfacial stability is mainly achieved through interfacial interactions and charge redistribution, rather than large-scale reconstruction. The calculated binding energies marked in the figure above reveal the different interaction strengths among the three heterostructures. The Si_3N_4-G heterostructure has the most negative binding energy ($E_b = -3.062$ eV), indicating its strongest interfacial bonding, followed by the AlN-G heterostructure ($E_b = -2.241$ eV). In contrast, the BN-G heterostructure has a relatively small negative binding energy ($E_b = -1.773$ eV), indicating weaker interfacial affinity under the same model construction and calculation settings. This trend indicates that although all three nitrides can form stable heterostructures with graphene, their interfacial coupling strengths are not identical, but rather depend on the intrinsic electronic structure and surface polarity of the nitride layers. The figure below shows the side view structure and the charge density difference iso-surface, visually illustrating the redistribution of electrons during heterojunction formation. Overall, the charge density difference spectrum shows complementary charge accumulation and depletion regions concentrated near the interface, indicating that interfacial contact induces electron rearrangement and polarization. This

redistribution is particularly pronounced near the interface atoms and on the graphene basal surface directly beneath the nitride layer, reflecting the formation of interfacial dipoles and the establishment of polarized interfaces.

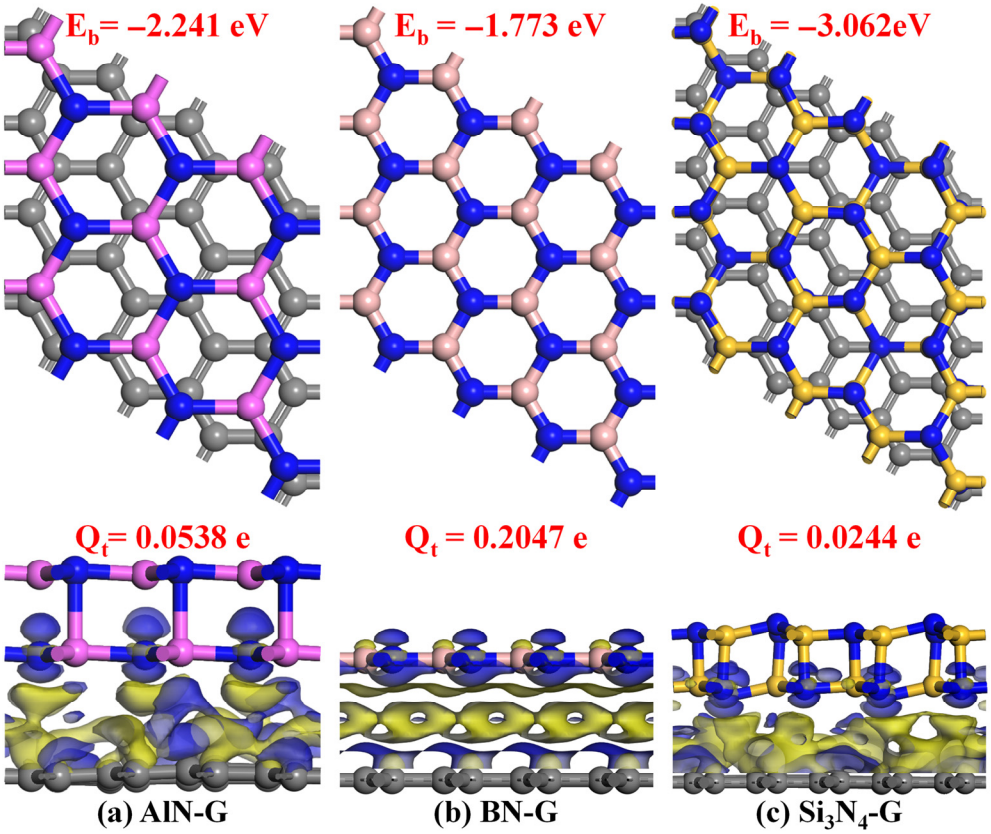

Figure 7. Optimized atomic structures and interfacial charge redistribution of graphene/nitrides heterojunctions obtained from DFT calculations. The upper panels show the top-view geometries of three representative graphene-nitrides heterostructures (left to right), with the corresponding binding energies labeled. The lower panels present the side-view structures together with the charge-density difference surfaces at the interface, where charge accumulation and depletion regions are indicated by different colors. The net interfacial charge transfer for each heterojunction is also given.

The net interfacial charge transfer value (Q_t) further supports these observations, with the BN-G heterojunction exhibiting the largest charge transfer (Q_t = 0.2047 e), indicating the highest degree of electron redistribution between the graphene and nitride components among the three systems. In comparison, the AlN heterojunction exhibits a moderate charge transfer (Q_t = 0.0538 e), while the Si_3N_4-G heterojunction shows the smallest net charge transfer (Q_t = 0.0244 e). This comparison indicates that the bonding strength and net charge transfer are not necessarily linearly related; heterojunctions may exhibit strong interfacial bonding (more negative Eb) but relatively small net charge transfer because their stability may also stem from short-range electrostatic interactions and interfacial polarization, which do not necessarily translate into a large net electron transfer. The interfacial charge redistribution shown in Figure 7 suggests that the graphene/nitride interface can serve as an effective polarization center. The coexistence of charge accumulation/depletion regions indicates the formation of interfacial dipoles and enhanced local electric field modulation, which can promote Maxwell–Wagner–Sillars-type interfacial polarization when such heterojunction fillers are embedded in a polymer matrix. Therefore, even though the macroscopic dielectric and sensing differences among the three nitride-based composites are not significant, the DFT calculations provide microscopic evidence that the

graphene/nitride interface itself supports interfacial polarization and charge accumulation, consistent with the experimentally observed enhancements in dielectric constant and induced voltage output.

Figure 8 illustrates the electronic band structures of monolayer nitrides and their graphene/nitride heterojunctions. Figure 8a–c show the intrinsic band structures of monolayers AlN, BN, and Si3N4, respectively, while Figure 8d–f correspond to the band structures of the AlN-G, BN-G, and Si_3N_4-G heterostructures, respectively. These three nitride monolayers are typical wide-bandgap semiconductors. The calculated bandgap for AlN is 4.518 eV, and for BN it is 4.647 eV, indicating that their intrinsic electronic conductivity is very limited at room temperature. In contrast, while Si_3N_4 has a smaller bandgap, its value is still relatively large at 2.772 eV. This larger bandgap confirms that, in the absence of graphene, these nitride layers are electronic insulators, expected to contribute primarily to dielectric polarization rather than free carrier transport. When the three nitrides were stacked with graphene, the band structure of the heterojunctions exhibited distinct graphene-derived band characteristics near the Fermi level. Bands appeared near the Fermi level in all three heterojunctions, indicating a significant change in the electronic states near the Fermi level compared to isolated nitride layers. This phenomenon is consistent with the formation of heterojunction interfaces and interfacial coupling between conductive graphene sheets and wide-bandgap nitride layers. In all three systems, BN-G showed a small but discernible bandgap of approximately 0.101 eV. This bandgap opening suggests that interfacial interactions and symmetry breaking in the heterostructure slightly perturb the Dirac dispersion of graphene, leading to weaker semiconductor properties rather than the ideal bandgap-free characteristics of graphene. For AlN-G and Si_3N_4-G, the overall band structure also indicates a strong graphene-related contribution near the Fermi level, although the degree of band gap opening and band distortion differs from that of BN-G. This reflects the differences in interfacial coupling strength and charge redistribution behavior among different nitride species. It is important to emphasize that the small band gap (0.101 eV) mentioned here is not intended to suggest that thermally activated body conduction is dominant at room temperature. Rather, the key significance of Figure 8 is that the graphene/nitride interface alters the electronic structure near the Fermi level, which can promote interfacial charge redistribution and enhance the ability of the heterostructure to accumulate charge under an external electric field. In polymer composites, this microscopic interfacial electronic modulation can translate into stronger Maxwell–Wagner–Siralls-type interfacial polarization and improved induced voltage response, consistent with the experimentally observed enhancements in dielectric constant and electric field-induced output.

Figure 9 compares the total density of states (TDOS) of three graphene/nitride heterojunction systems (black curves) with their corresponding isolated components (i.e., pristine nitride monolayers (red) and graphene (blue)). The Fermi level is located at 0 eV (vertical dashed line). Overall, the TDOS of each heterostructure is not a simple arithmetic superposition of its components; instead, significant changes in peak position and intensity are observed, indicating interfacial electronic coupling and charge redistribution during stacking. For isolated AlN, the density of states near the Fermi level is largely suppressed, consistent with the wide bandgap characteristics of AlN. In contrast, graphene contributes a limited density of states near the Fermi level. After AlN and graphene form a heterojunction, the TDOS near the Fermi level is more significant compared to isolated nitrides and deviates significantly from the density of states distribution of pure graphene, including an enhanced feature in the near-Fermi level region. These changes indicate that the graphene-derived states are perturbed by AlN, and interfacial coupling alters the

electronic environment at the interface, thereby promoting charge accumulation under external fields.

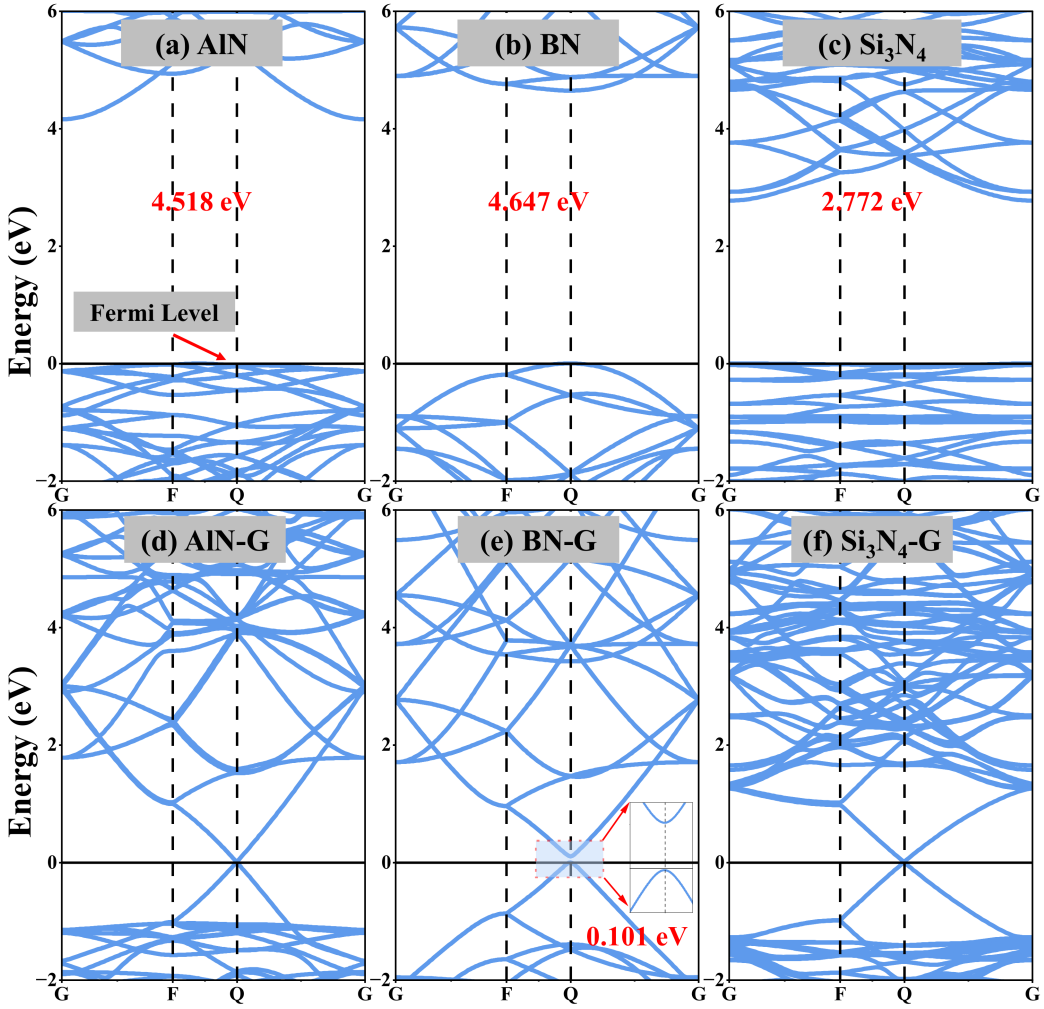

Figure 8. Band structures obtained from DFT calculations. (**a**–**c**): Intrinsic band structures of monolayer AlN, BN, and Si_3N_4, respectively, showing their intrinsic band gaps. (**d**–**f**): Band structures of the corresponding graphene/nitrides heterojunctions (AlN-G, BN-G, and Si_3N_4-G).

Similarly, due to the larger band gap, the density of states (DOS) of pristine BN near the Fermi level is negligible, while graphene contributes the majority of the DOS near the electric field strength. The TDOS of the heterojunction exhibits significant reshaping characteristics near the Fermi level, with its peak shape altered compared to that of isolated graphene. Notably, the TDOS near the Fermi level in the BN-G heterostructure shows strong modulation, consistent with the small band gap opening observed in the corresponding band structure (Figure 8e). This indicates that the electronic states of graphene are more strongly perturbed in BN-G, reflecting enhanced interfacial coupling and symmetry breaking when graphene is stacked with BN. For pristine Si_3N_4, the TDOS near the Fermi level is again suppressed, reflecting its semiconductor properties. After stacking with graphene, the TDOS distribution of the heterojunction changes compared to individual components, including broadening and redistribution over a wider energy range. Although graphene remains the major contributor near the Fermi level, the significant reshaping and broadening of the heterojunction TDOS indicates interfacial interactions and electron redistribution between graphene and the Si_3N_4 layer. In summary, the TDOS results demonstrate that the introduction of a nitride layer can significantly perturb the electronic structure of graphene, particularly near the Fermi level, leading to a redistribution of

interfacial states. This near-field electronic modulation is crucial from the perspective of the dielectric and electric field-induced response of the polymer composite, as it affects charge storage and interfacial polarization behavior. The change in the density of states near the Fermi level can promote charge accumulation at the heterojunction interface and enhance Maxwell–Wagner–Sillars-type interfacial polarization. This microscopic evidence supports the experimentally observed enhancement of the dielectric constant and the modest but sustained increase in the normalized induced voltage response after incorporation of graphene/nitride heterojunction filler. Further comparison of the microscopic mechanisms revealed by DFT regarding electronic and structural contributions helps to understand why different nitrides exhibit similar macroscopic dielectric enhancement. While the macroscopic outputs of the three systems tend to be consistent, the microscopic driving forces differ significantly. The BN-G system exhibits the highest interfacial charge transfer (Q_t = 0.2047 e) and a discernible bandgap opening (0.101 eV) in terms of the electronic-dominated mechanism. This suggests that its performance compensates for its weaker binding force through a strong "electronic modulation" mechanism, where the redistribution of the electron cloud determines the interfacial polarization. In contrast, the Si_3N_4-G system plays a crucial role in the structural-dominated mechanism, exhibiting extremely small charge transfer (0.0244 e) but the highest binding energy (E_b = −3.062 eV). This suggests the existence of a "structural anchoring" mechanism, where a thermodynamically rigid interface facilitates the consistent alignment of dipoles without requiring extensive electron exchange. This distinct "electronics vs. structure" dichotomy demonstrates the robustness of the heterojunction strategy: it provides a general design framework that allows for the modulation of dielectric response through strong electronic coupling (such as BN-G) or superior structural stability (such as Si_3N_4-G) to achieve the same sensing objective.

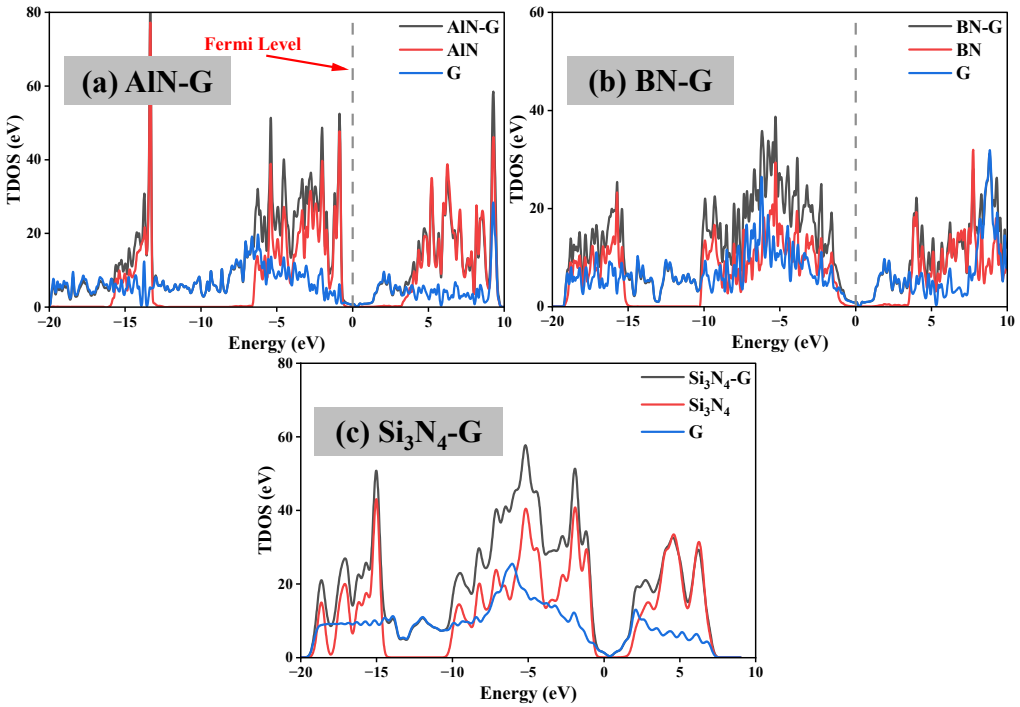

Figure 9. Total density of states (TDOS) of the three graphene/nitrides heterojunction systems and their individual components: (**a**) AlN-G, (**b**) BN-G, and (**c**) Si_3N_4-G. In each panel, the TDOS of the heterojunction (black) is compared with those of the corresponding pristine nitrides layer (red) and graphene (blue). The Fermi level is set to 0 eV and is indicated by the vertical dashed line.

4. Conclusions

This study synthesized graphene/nitride heterojunction powders (AlN-G, BN-G, and Si_3N_4-G) via a hydrothermal method and incorporated them into a PDMS matrix to prepare flexible composite films. The main conclusions are summarized below:

(i) Scanning electron microscopy (SEM) revealed that the three fillers exhibited different morphological characteristics, indicating different interfacial contact modes within the PDMS. EDS energy dispersive spectroscopy and elemental mapping further confirmed the coexistence and spatial co-distribution of carbon with the corresponding nitride elements (Al/B/Si and N), supporting the successful construction of the graphene-nitride heterojunction powders.

(ii) Dielectric spectroscopy analysis showed that all samples exhibited typical dielectric dispersion characteristics of polymer composites. Compared with pure PDMS, the dielectric constant was significantly improved within the measured frequency range after the introduction of graphene and graphene/nitride heterojunction fillers. The loss tangent also decreased with increasing frequency, and the curve was smooth without any abnormal relaxation peaks. Notably, the tanδ trends of the introduced heterojunction composites remain similar, indicating that under the same loading and processing conditions, the overall dielectric loss is mainly determined by the PDMS matrix and common interfacial relaxation mechanisms, while the extracted dielectric descriptors reveal consistent trend-level differences dependent on the nitride species, confirming the distinct role of filler identity even within a matrix-dominated response.

(iii) Under the same testing and normalization scheme (PDMS = 1.00), the introduction of graphene/nitride heterojunction fillers leads to further performance improvements, with Si_3N_4-G/PDMS showing the highest value among all tested systems, at 1.07447 (≈7.447%). Under the current composite formulation, heterojunction engineering can provide stable and repeatable performance improvements, and the systematic variations among the three nitrides confirm that the enhancement is tunable based on the specific microscopic mechanism (electronic vs. structural).

(iv) Theoretical calculations show that all three nitrides and graphene can form stable heterojunction structures. The calculated binding energies indicate different coupling strengths: Si_3N_4-G (E_b = −3.062 eV) > AIN-G (−2.241 eV) > BN-G (−1.773 eV). Mulliken population analysis revealed charge transfer at the interface, with magnitudes following the order BN-G (Q_t = 0.2047 e) > AlN-G (0.0538 e) > Si_3N_4-G (0.0244 e). The charge density difference and total density of states (TDOS) results together indicate that nitride stacking perturbs the electronic states of graphene near the Fermi level and promotes the formation of interfacial polarization centers, providing a microscopic explanation for the experimentally observed increase in dielectric constant and enhanced electric field-induced voltage response. In summary, the combination of dielectric spectroscopy, electric field-sensing measurements, and DFT analysis demonstrates that graphene/nitride heterojunction fillers can simultaneously improve the dielectric constant and enhance electric field-sensing output while keeping dielectric loss within a controllable range. This provides a practical and mechanistically explainable strategy for flexible dielectric layers in electric field-sensing applications.

Author Contributions: B.L., writing—original draft preparation, J.S., data curation, Y.L., formal analysis, T.J., methodology, H.Y., software. All authors have read and agreed to the published version of the manuscript.

Funding: This work is supported by the Science and Technology Project of China Southern Power Grid Co., Ltd. (YNKJXM20240021, YNKJXM20240047).

Data Availability Statement: The data presented in this study are available on request from the corresponding author.

Conflicts of Interest: Bo Li, Yuxing Lei, and Tingting Jiang were employed by the Electric Power Research Institute of Yunnan Power Grid Co., Ltd., Jiao Sun was employed by the Kunming Power Supply Bureau of Yunnan Power Grid Co., Ltd. The remaining authors declare that the research was conducted in the absence of any commercial or financial relationships that could be construed as a potential conflict of interest.

References

1. Tan, X.; Zhang, W.; He, M.; Li, W.; Ao, G.; Zhou, F. Non-Contact Adaptive Voltage Sensor Based on Electric Field Coupling Principle. *Sensors* **2023**, *23*, 8316. [CrossRef] [PubMed]
2. Peng, H.; Liu, H.; Shang, K.; Li, G.; Zhao, L. Design and Simulation Test of Non-Contact Voltage Sensor. *Sensors* **2025**, *25*, 3118. [CrossRef] [PubMed]
3. Shen, J.; Liu, L.; Li, X.; Tu, Y.; Liu, B.; Deng, S.; Yang, X. A novel non-contact voltage measurement based on distribution lines. *IET Gener. Transm. Distrib.* **2025**, *19*, e13336. [CrossRef]
4. Xia, X.; Zhong, Z.; Weng, G.J. Maxwell–Wagner–Sillars mechanism in the frequency dependence of electrical conductivity and dielectric permittivity of graphene-polymer nanocomposites. *Mech. Mater.* **2017**, *109*, 42–50. [CrossRef]
5. Samet, M.; Levchenko, V.; Boiteux, G.; Seytre, G.; Kallel, A.; Serghei, A. Electrode polarization vs. Maxwell-Wagner-Sillars interfacial polarization in dielectric spectra of materials: Characteristic frequencies and scaling laws. *J. Chem. Phys.* **2015**, *142*, 194703. [CrossRef]
6. Samet, M.; Kallel, A.; Serghei, A. Maxwell-Wagner-Sillars interfacial polarization in dielectric spectra of composite materials: Scaling laws and applications. *J. Compos. Mater.* **2022**, *56*, 3197–3217. [CrossRef]
7. Wang, H.; Yang, L. Dielectric constant, dielectric loss, conductivity, capacitance and model analysis of electronic electroactive polymers. *Polym. Test.* **2023**, *120*, 107965. [CrossRef]
8. Ferrari, A.C.; Bonaccorso, F.; Fal'Ko, V.; Novoselov, K.S.; Roche, S.; Bøggild, P.; Borini, S.; Koppens, F.H.; Palermo, V.; Pugno, N.; et al. Science and technology roadmap for graphene, related two-dimensional crystals, and hybrid systems. *Nanoscale* **2015**, *7*, 4598–4810. [CrossRef]
9. Lee, S.J.; Yoon, S.J.; Jeon, I.Y. Graphene/polymer nanocomposites: Preparation, mechanical properties, and application. *Polymers* **2022**, *14*, 4733. [CrossRef]
10. Xiao, K.; Wang, W.; Wang, K.; Zhang, H.; Dong, S.; Li, J. Improving triboelectric nanogenerators performance via interface tribological optimization: A review. *Adv. Funct. Mater.* **2024**, *34*, 2404744. [CrossRef]
11. Huang, X.; Jiang, P.; Tanaka, T. A review of dielectric polymer composites with high thermal conductivity. *IEEE Electr. Insul. Mag.* **2011**, *27*, 8–16. [CrossRef]
12. Wang, Z.; Iizuka, T.; Kozako, M.; Ohki, Y.; Tanaka, T. Development of epoxy/BN composites with high thermal conductivity and sufficient dielectric breakdown strength partI-sample preparations and thermal conductivity. *IEEE Trans. Dielectr. Electr. Insul.* **2011**, *18*, 1963–1972. [CrossRef]
13. Wang, Z.; Wang, X.; Wang, S.; He, J.; Zhang, T.; Wang, J.; Wu, G. Simultaneously enhanced thermal conductivity and dielectric breakdown strength in sandwich AlN/epoxy composites. *Nanomaterials* **2021**, *11*, 1898. [CrossRef] [PubMed]
14. Chen, M.; Zhou, W.; Zhang, J.; Chen, Q. Dielectric property and space charge behavior of polyimide/silicon nitride nanocomposite films. *Polymers* **2020**, *12*, 322. [CrossRef]
15. Zhi, C.; Bando, Y.; Tang, C.; Kuwahara, H.; Golberg, D. Large-scale fabrication of boron nitride nanosheets and their utilization in polymeric composites with improved thermal and mechanical properties. *Adv. Mater.* **2009**, *21*, 2889–2893. [CrossRef]
16. Wang, E.; Lu, X.; Ding, S.; Yao, W.; Yan, M.; Wan, G.; Deng, K.; Wang, S.; Chen, G.; Ma, L.; et al. Gaps induced by inversion symmetry breaking and second-generation Dirac cones in graphene/hexagonal boron nitride. *Nat. Phys.* **2016**, *12*, 1111–1115. [CrossRef]
17. Kharche, N.; Nayak, S.K. Quasiparticle band gap engineering of graphene and graphone on hexagonal boron nitride substrate. *Nano Lett.* **2011**, *11*, 5274–5278. [CrossRef]
18. Ramasubramaniam, A.; Naveh, D.; Towe, E. Tunable band gaps in bilayer graphene− BN heterostructures. *Nano Lett.* **2011**, *11*, 1070–1075. [CrossRef]
19. Zollner, K.; Cummings, A.W.; Roche, S.; Fabian, J. Graphene on two-dimensional hexagonal BN, AlN, and GaN: Electronic, spin-orbit, and spin relaxation properties. *Phys. Rev. B* **2021**, *103*, 075129. [CrossRef]
20. Liu, X.; Zhang, Z.; Luo, Z.; Lv, B.; Ding, Z. Tunable electronic properties of graphene/g-AlN heterostructure: The effect of vacancy and strain engineering. *Nanomaterials* **2019**, *9*, 1674. [CrossRef]

21. Liu, X.; Zhang, Z.; Lv, B.; Ding, Z.; Luo, Z. The external electric field-induced tunability of the Schottky barrier height in graphene/AlN interface: A study by first-principles. *Nanomaterials* **2020**, *10*, 1794. [CrossRef] [PubMed]
22. Guo, Y.; Zhang, S.; Wang, Q. Electronic and optical properties of silicon based porous sheets. *Phys. Chem. Chem. Phys.* **2014**, *16*, 16832–16836. [CrossRef] [PubMed]
23. Shivani, V.; Sriram, S. Ab Initio Study of Two-dimensional β-Si3N4 Monolayer as a Promising Anode for Sodium-ion Batteries. *Surf. Interfaces* **2025**, *72*, 107044. [CrossRef]
24. Zhao, L.; Xu, S.; Wang, M.; Lin, S. Probing the thermodynamic stability and phonon transport in two-dimensional hexagonal aluminum nitride monolayer. *J. Phys. Chem. C* **2016**, *120*, 27675–27681. [CrossRef]
25. Pakdel, A.; Zhi, C.; Bando, Y.; Golberg, D. Low-dimensional boron nitride nanomaterials. *Mater. Today* **2012**, *15*, 256–265. [CrossRef]
26. Delley, B. An all-electron numerical method for solving the local density functional for polyatomic molecules. *J. Chem. Phys.* **1990**, *92*, 508–517. [CrossRef]
27. Delley, B. From molecules to solids with the DMol3 approach. *J. Chem. Phys.* **2000**, *113*, 7756–7764. [CrossRef]
28. Kohn, W.; Sham, L.J. Self-consistent equations including exchange and correlation effects. *Phys. Rev.* **1965**, *140*, A1133. [CrossRef]
29. Perdew, J.P.; Burke, K.; Ernzerhof, M. Generalized gradient approximation made simple. *Phys. Rev. Lett.* **1996**, *77*, 3865. [CrossRef]
30. Delley, B. Hardness conserving semilocal pseudopotentials. *Phys. Rev. B* **2002**, *66*, 155125. [CrossRef]
31. Grimme, S. Semiempirical GGA-type density functional constructed with a long-range dispersion correction. *J. Comput. Chem.* **2006**, *27*, 1787–1799. [CrossRef]
32. Grimme, S.; Antony, J.; Ehrlich, S.; Krieg, H. A consistent and accurate ab initio parametrization of density functional dispersion correction (DFT-D) for the 94 elements H-Pu. *J. Chem. Phys.* **2010**, *132*, 154104. [CrossRef]
33. Monkhorst, H.J.; Pack, J.D. Special points for Brillouin-zone integrations. *Phys. Rev. B* **1976**, *13*, 5188. [CrossRef]
34. Mermin, N.D. Thermal properties of the inhomogeneous electron gas. *Phys. Rev.* **1965**, *137*, A1441. [CrossRef]
35. Giovannetti, G.; Khomyakov, P.A.; Brocks, G.; Kelly, P.J.; Van Den Brink, J. Substrate-induced band gap in graphene on hexagonal boron nitride: Ab initio density functional calculations. *Phys. Rev. B—Condens. Matter Mater. Phys.* **2007**, *76*, 073103. [CrossRef]
36. Björkman, T.; Gulans, A.; Krasheninnikov, A.V.; Nieminen, R.M. van der Waals Bonding in Layered Compounds from Advanced Density-Functional First-Principles Calculations. *Phys. Rev. Lett.* **2012**, *108*, 235502. [CrossRef]
37. Mulliken, R.S. Electronic population analysis on LCAO–MO molecular wave functions. I. *J. Chem. Phys.* **1955**, *23*, 1833–1840. [CrossRef]

Disclaimer/Publisher's Note: The statements, opinions and data contained in all publications are solely those of the individual author(s) and contributor(s) and not of MDPI and/or the editor(s). MDPI and/or the editor(s) disclaim responsibility for any injury to people or property resulting from any ideas, methods, instructions or products referred to in the content.